Thermal Satellite Imagery Analysis and Emissivity Characteristics for the Prediction of Oil Reservoirs Existence

Ali Badri Tarish
Dept. of Computer & Communication
Systems Engineering, UPM
Serdang, Selangor, Malaysia
gs56905@student.upm.edu.my

Aduwati Sali
WiPNET Research Centre, Dept. of
Computer & Communication Systems
Engineering, UPM, Serdang,
Selangor, Malaysia
aduwati@upm.edu.my

Abdul Rashid Mohamed Shariff
Dept. of Biological & Agricultural
Engineering, UPM, Serdang,
Selangor, Malaysia
rashidpls@upm.edu.my

Marsyita Hanafi
Dept. of Computer & Communication
Systems Engineering, UPM
Serdang, Selangor, Malaysia
marsyita@upm.edu.my

Alyani Ismail
Dept. of Computer & Communication
Systems Engineering, UPM
Serdang, Selangor, Malaysia
alyani@upm.edu.my

Intehaa A. Mohammed
Dept. of Physics, College of Education
for Pure Sciences, UOB
Babylon, Iraq
intehaa.mohammed@uobabylon.edu.iq

Abstract— Simultaneous transformation of natural land cover contributes significantly to changing the surface phenomena making accurate forecasting difficult. Ground surveys would permit Land Use Land Cover (LULC) classification, but they are burdensome, expensive, and time-consuming and lacks accuracy in the exploration for all target areas at the same time, which highlights satellite imagery an evident and preferred alternative. A new mathematical method has been used for calculating the highest and lowest Land Surface Temperature (LST) to improve model accuracy for a particular location and detect oil seep-induced alteration from Landsat Data Continuity Mission (LDCM). Two sites within different patterns were chosen to represent a diversity of thermal anomalies positions in the study area. The results show that there are no traces of oil in either zone 1 lies which in the Kanoya province and zone 2 located east of the coast of Kagoshima which is overlooking the Pacific Ocean. In the end, the night-time scenes of the Thermal Infrared Sensor (TIRS) achieve a high gain of the thermal image with radiance 3.2-12.65 (Watts/m^2 sr µm). Moreover, the analysis of the (TIRS) image is an optimal explanation for geomorphology and subsurface geology in southern Japan via the potentiality of the simulators set.

Keywords— Exploration; Microseepage; Thermal sensors; Emissivity; Brightness Temperature; Land Surface Temperature

I. INTRODUCTION

The surface anomalies of oil represents the surface expression of the migration path, where oil will flow on both sides of this path driven from the ground. These surface features are evidence of the presence of oil reservoirs at the bottom [1]. Based on previous satellite observations, several methods have been applied to calculate air pollutant emissions from point sources, as methane emissions associated with oil extraction operations [2]. The presence of chemical elements leaking out of oil tanks, and elements already present in the surface leads to a change in the color of the surface from red to green/gray due to change ferric turns into ferrous oxide (FeO) [3]. Also other indications of the presence of oil when the formation of cement carbonates such as calcite. Through the analysis of spectral signals in the multispectral window of the short wave of the electromagnetic spectrum can determine the spectrum of carbon cement which is another proof of the presence of oil [4]. Fig.1 illustrates the seepage paths and surface alterations. Space technology is, therefore, a useful tool for identifying potential surface phenomena due to the microseepage of natural oil. Satellite technology is one of the most important modern methods used in the exploration of oil, where satellite images are capable of providing rapid initial analysis of the oil presence at low cost [5]. The schematic in Figure 1 shows that extrusive, intrusive igneous, hydrothermal fluids, oil, and chemically active volatiles travel convectively through fault zones and rock units that have high permeability at the time of intrusion. The hot spots could be promising spots for oil production [6]. The hydrocarbon drain light is almost vertical in the gaseous phase, leading to a shallow anomaly near-surface microbial, geochemical, and alteration anomaly above petroleum accumulation (directly above -apical or spill point-halo). Fig. 1 illustrates the microseepage model with the geochemical-geophysical specifications [7].
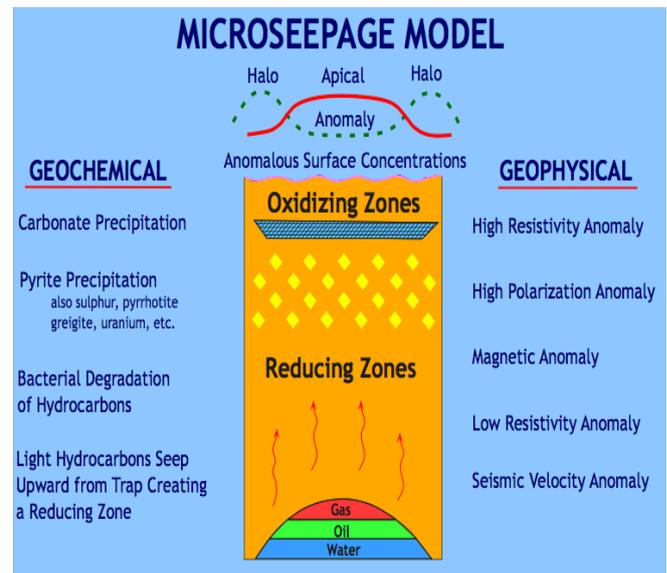
Fig. 1. Microseepage model process and its surface effects [7]

Microseepage systems can be tracked at different levels through satellite data, as an integrated spectral approach can be relied upon, to investigate the quantity, variability, and physiochemistry of minerals diagenetically induced via an a ctive-microseepage system [8]. Tectonic structures are subject to crustal expansion and lithosphere thinning and are associated with structurally controlled heat transfer and fluid flow. In seismically active regions, temporal changes of geothermal system properties as namely temperature, and geochemistry are the cause for changes in subsurface chemical and physical processes, such as

microfracture, fluid mixing, occasional gas injection into the hydrothermal system, and permeabil ity changes [9].

II. GEOLOGIC BACKGROUND

The land cover of the study area consists of several geological formations, the Shimanto belt (SM) is Paleogene accretionary complex since the Cretaceous dominates its turbidite, limestone, and less chert. Along the Nankai trough, the Neogene components to quaternary accretionary complexes are mainly exposed offshore, except for the southern margin of the Kanto area and the southern margin of Shikoku [10]. The area, as shown in Fig. 2 was covered by a satellite scene for LDCM. Recently, the possibility of mapping thermal anomalies has increased, which means increased interest in energy resources [11].
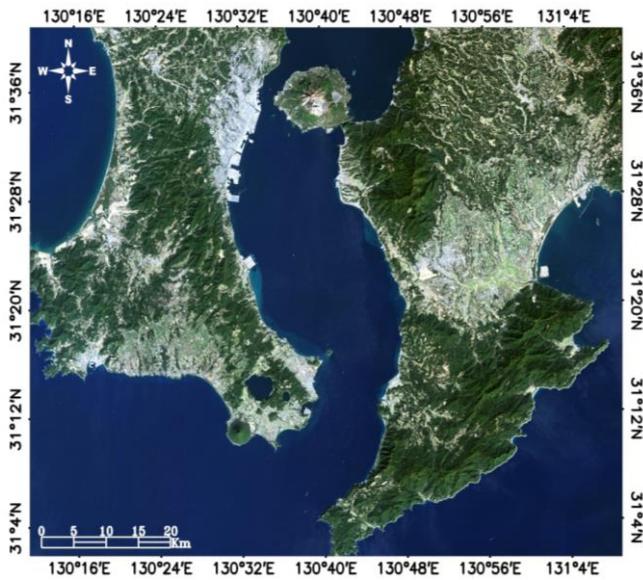
Fig. 2. The truth colour composite (RGB) of the ROI.

Table I represents the area of the region of interest (ROI) and the coordinates of the upper left point and lower right point.

TABLE I.   The specifications of ROI

Area		6596.179 Km²
Upper Left (UL)	Latitude	31º 40' 48.08" N
	Longitude	130º 11' 42.83" E
Lower Right (LR)	Latitude	31º 1' 12.05" N
	Longitude	131º 8' 50.13" E

In this research, the aim of the work was to identify the anomalies of the thermal spectrum in the target area. Through the change in (LST) values, which indicates the most promising sites for the development of thermal-energy fields. Also, to classify the oil seep-induced alteration via LDCM and explore the potential of thermal imagery for the different types of seeps and characterization of geophysical and spectral maps in the study area.

III. METHODOLOGY

The overall methodology applied is commensurate with the era of modern exploration of oil. The overall methodology flowchart is depicted in Fig. 3 shows that the stages of dealing with the thermal bands 10 and 11 and then the classification of each image produced by the conversions within the

application of mathematical algorithms leads to special access to the desired areas of thermal anomalies. The first step begins with collecting data from the satellite and available geophysical information about the study area. All of the objects, which have a temperature greater than absolute zero, can be emitting thermal infrared energy. This energy can be measured through acquisition, processing, and interpretation of the thermal radiation data within the thermal infrared (TIR) region of the electromagnetic (EM) radiation using thermal satellite imagery, when radiation emitted from the target surface is measured, reversing images of optical satellites that measure radiation reflected from the target surface. The basis of thermal sensors is recording the radiation temperatures of ground materials, which are related to the surface kinetic temperature (T_{kin}) and emissivity (ε). The key of the thermal image expresses the surface radiant temperature, where the colder areas are dark while the warmer areas are light. The thermal anomalies that occur caused by differences from surface temperature can be exploited for exploration of the hydrocarbon microseepage.
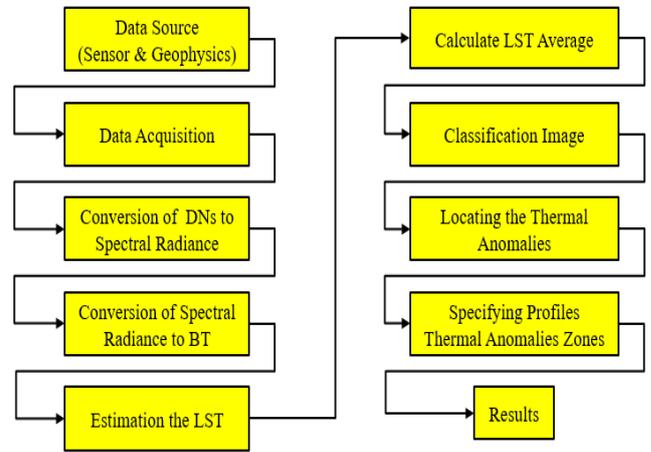
Fig. 3. The flowchart of exploration simulation data in this study

A. Thermal Infrared Sensor (TIRS)

TIRS is a push-broom sensor utilizing a focal plane with long arrays of photosensitive detectors. TIRS utilizes Quantum Well Infrared Photo-detectors (QWIPs) to measure long-wave Thermal Infrared (TIR) energy emitted from the earth's surface that is the intensity of which is a function of surface temperature [12]. These detectors (QWIPs) are sensing two thermal infrared wavelength bands, band 10 and band 11, allowing for separation of the earth's surface temperature from that of the atmosphere. QWIP's styling works on the complex fundamentals of quantum mechanics. The sensor works in a push-broom imaging pattern to obtain earth data in two thermal infrared channels [13], [14]. The temporal resolution of the (LDCM) is 16-days. The LDCM scene has a 185 km swath width. (TIRS) that is sensing the wavelengths which are in the thermal infrared region given in Table II.

TABLE II.   (TIRS) BANDS PROPERTIES

Instrument	Band	Spectral Range	Spatial Resolution
TIRS	10	10.6 - 11.19 µm	30 m
	11	11.5 - 12.51 µm	30 m

B. Spectral Emissivity and Kinetic Temperature

Radiation emitted from ground objects is measured to estimate the temperature. This mensuration gives the radiant temperature of an object by depending on two factors kinetic temperature and emissivity [15]. Emissivity is the emitting capacity from a real substance compared to the emitting capacity from the black body. In addition, it is a spectral property that changes with the composition of substance and geometrical arrangement of the surface [16]. Emissivity, symbolized by epsilon (ε), differs from 0 to 1. If it equal to 1, the object has thermal behavior similarity to that of a black body. Kinetic temperature is the surface temperature of an object/earth and is a measurement of the amount of heat energy include in it. It is measured by several units, like in degrees Kelvin (°K), degrees Centigrade (°C), and degrees Fahrenheit (°F) [17].

C. The Wien Displacement Law and Black Body Emissivity Effect

The blackbody can be defined physically as a hypothetical body that absorbs and emitted all incident energy at all wavelengths. That is meaning the substances are emitting the thermal radiation in amounts dependent on substances properties as internal temperature and emissivity [18].

Planck's law of blackbody radiation gives the relationship of electromagnetic radiation emitted from the black body at a wavelength λ as a function for absolute temperature. This is done by defining the spectral radiance L_λ such that the radiance ΔL included in a small domain of wavelengths $\Delta\lambda$ is given by:

$$\Delta L = L_\lambda\, \Delta\lambda \tag{1}$$

Where:

L_λ: Spectral radiance (W/(m^2 * sr * μm))

λ: wavelength (μm)

Using quantum mechanics, where the following relationship was found:

$$L_\lambda = \frac{2hc^2}{\lambda^5(e^{\left(\frac{hc}{\lambda KT}\right)}-1)} \tag{2}$$

Where:

h: Planck constant = 6.626 x 10^{-34} J.sec

k: Boltzmann constant = 1.38 x 10^{-23} J/ °K

c: Speed of light = 3*10^8 m sec^{-2}

T: Blackbody temperature (°K)

The spectrum of the blackbody is characterized by its specialized frequency, and since the frequency increases with increasing temperature, most of the emitted radiation is in the infrared region of the electromagnetic spectrum [19]. The black body emits radiation which has a continuous distribution of emitted wavelength as illustrated in Fig. 4. Where each curve gives the radiance L in dimensions of power per unit area multiplicand with the wavelength and the solid angle (Watts/m^2 sr μm) [20]. Equation (2) can be approximated as:

$$L_\lambda \approx \frac{2kT}{\lambda^4} \tag{3}$$

This is called the Rayleigh-Jeans approximation and it is matching to the right-hand portion of Fig. 4. The Planck formula can be integrated for calculating the blackbody total radiance over all wavelengths as shown [21]:

$$L = \int_0^\infty L_\lambda d\lambda = \frac{2\pi^4 k^4}{15c^2 h^3}T^4 \tag{4}$$
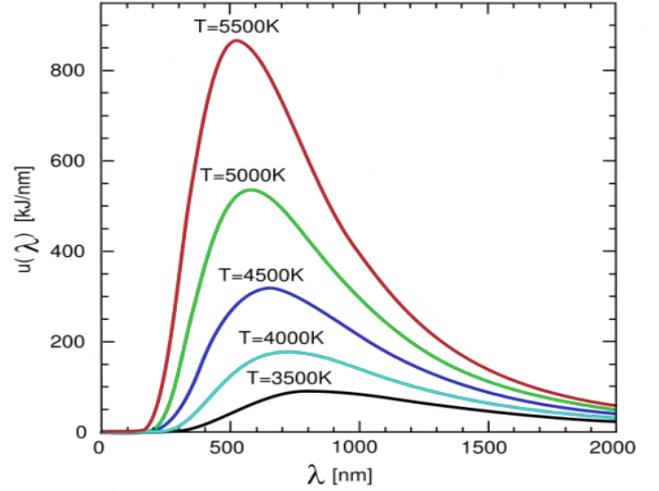
Fig. 4. Energy radiated of spectral distribution of blackbody for different temperatures [22]

The black body law Formula is the basic to define the emissivity (ε), the proportion between the spectral radiance of a given object (L_λ) and that of a blackbody at the same temperature ($L_{\lambda,P}$) (the 'P' denoted for 'Planck') [23]. This is given by the following equation:

$$L_\lambda = \varepsilon(\lambda)L_{\lambda,P} \tag{5}$$

The accurate solution for this equation to calculate amount of T is:

$$T = \frac{hc}{k\lambda\, ln(1+\frac{\exp(hc/\lambda kT_b)-1}{\varepsilon})} \tag{6}$$

If the emissivity (ε) is approaching to one then T can be approximated as:

$$T \approx \frac{T_b}{1+\frac{\lambda kT_b ln\varepsilon}{hc}} \tag{7}$$

IV. PROCEDURES AND RESULTS

The procedure consists of taking two different random locations on the result thermal image using a number of steps, then converting the Thermal Infrared Sensor (TIRS) raw data, in terms of Digital Numbers (DNs), to Land surface temperature (LST).

The raw data is acquired at night away from the incoming and exitance radiation of the shortwave that becomes zero after sunset [24]. The LST estimate using Landsat conversion DNs to physical units formulas using the parameters are given in equations (8, 9, and 10).

$$L_\lambda = ML * Qcal + A_L \qquad (8)$$

Where:

L_λ: Spectral radiance (W/(m² * sr * μm))

M_L: Radiance multiplicative scaling factor = 0.0003342

Q_{cal}: pixel value in DN

A_L: Radiance additive scaling factor = 0.1

$$T_B = \frac{K_2 (L_\lambda + 1)}{ln K_1} \qquad (9)$$

Where:

T_B: Brightness Temperature °K

K_1 and K_2: Band-specific thermal conversion constant from the metadata.

$$LST = \frac{T_B}{1 + \frac{\lambda k T_B ln\varepsilon}{hc}} \qquad (10)$$

LST: Land Surface Temperature °K

λ: Wavelength for band

K: Boltzmann's Constant = 1.38 x 10⁻²³ J/ °K

h: Plank's Constant = 6.626 x 10⁻³⁴ J.s

c: Velocity of Light 3 x 10⁸ m/s

ε: 0.96 [25]

Fig. 5. shows the raw data of TIRS images for band 10 and band 11 respectively. Fig. 6. shows the conversion dataset from digit numbers (DNs) values to spectral radiance values. Fig. 7. shows the conversion dataset from spectral radiance values to Top of Atmosphere (TOA) brightness temperature. Fig. 8. shows the conversion dataset from top (TOA) brightness temperature to Land Surface Temperature (LST), and Fig. 9. illustrates LST mean image. The results of the above procedures can be included in Table IV.
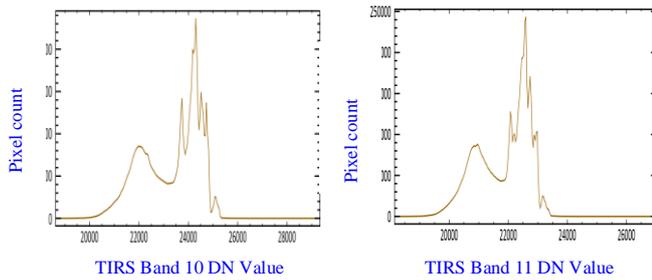
Fig. 5. Raw data of TIRS image bands 10 &11 histograms.
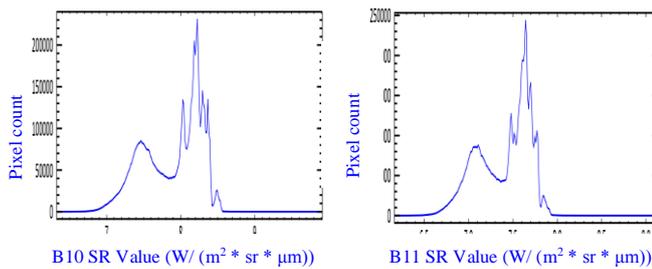
Fig. 6. TOA SR data of TIRS image bands 10 & 11 histograms.
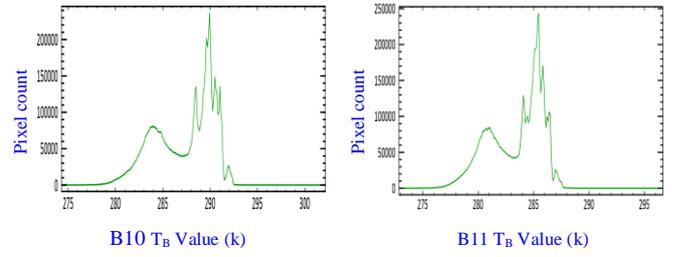
Fig. 7. TOA T_B data of TIRS image bands 10 &11 histograms.
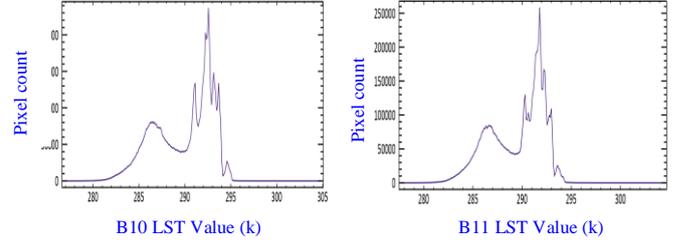
Fig. 8. LST data of TIRS image bands 10 &11 histograms.
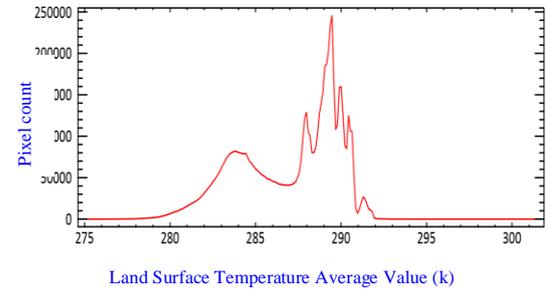
Fig. 9. LST mean image histogram.

TABLE III. DESCRIBES THE RESULTS OF THE FOUR PROCEDURES WITHIN THE SIMULATOR ENVIRONMENT.

Parameters \ Bands	Band 10	Band 11
DNs Value	24304	22595
Max. count pixel of DNs Value	236065	243232
S. R. Values (W/(m² * sr * μm))	8.22	7.64
Max. count pixel of S. R. Values	231148	244038
B. T. Values (°K)	289.94	288.92
Max. count pixel of B. T. Values	236679	257612
LST Values (°K)	292.57	291.79
Max. count pixel of LST Values	236540	258240
LST Average Value (°K)	289.47	
Max. count pixel of LST Average Value	245605	

The study area is classified according to the resulting LST averages values to extract the thermal anomalies using the density slice classification within the simulator environment. Temperature ranges are divided by color according to their values. The areas with the lowest temperatures take the blue color, ascending to areas where the temperatures are the highest values where they take the color magenta. The values that are confined between these ranges take arrangement from the cold colors to the warm colors which lie between the blue and magenta colors. Two random patterns of LSTs averages at different locations from the study area, in each one of these

patterns, takes the samples of LSTs averages using arbitrary profile within simulator environment, for inside and outside of thermal anomaly (the pattern). After that, it is calculated the change of LSTs averages between the points along with the profile that located inside and outside the thermal anomaly (ΔT) by calculating the average value of LSTs averages inside the profile (T_2) and the average value of LSTs averages outside the profile (T_1), and the locations of the profiles in the density slice classification of LST averages shown in the thermal anomalies map of the studied area in Fig. 10.
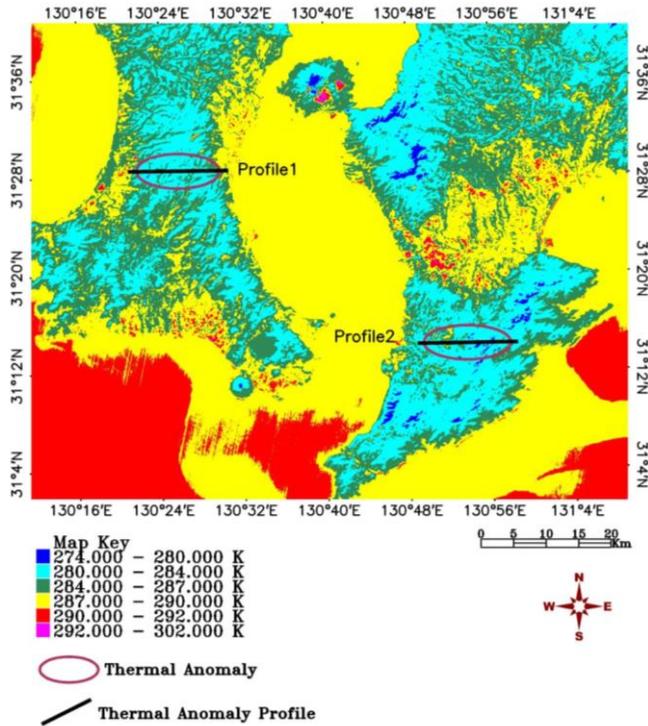
Fig. 10. The density slice classification of Land surface temperatures averages with thermal anomalies map of the studied area.

The first thermal anomaly (Profile1) lies in the Kanoya province, and consists of mountainous forests, a number of scattered farms within the thermal anomaly zone, and two villages on the boundaries of the thermal anomaly zone, where the temperatures in this zone are different from the surrounding areas. Fig. 11 is displaying the land surface temperatures (LSTs) averages values on the length of the profile1 inside the thermal anomaly region (T_2) where its value is 283.5131924 °K and the land surface temperatures (LSTs) averages values on the length of the profile1 outside the thermal anomaly region (T_1) value is 287.2096651°K, therefore the (ΔT) in this zone was -3.6964727 °K.
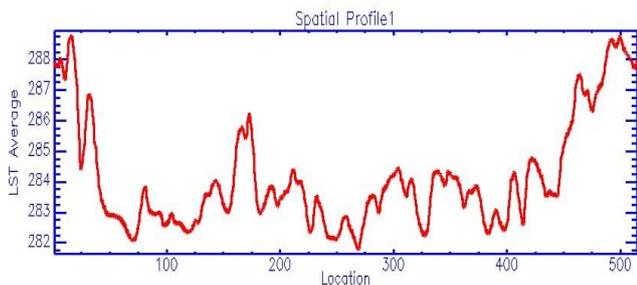
Fig. 11. Land surface temperature average change along on the Profile1

The second thermal anomaly (Profile2) lies located east of the coast of Kagoshima which is overlooking the Pacific Ocean. The temperatures in this zone are different from the surrounding areas. Fig. 12 is displaying the land surface temperatures (LSTs) averages values on the length of the profile1 inside the thermal anomaly region (T_2) where its value is 282.6721610 °K and the land surface temperatures (LSTs) averages values on the length of the profile1 outside the thermal anomaly region (T_1) value is 283.4496575 °K, therefore the (ΔT) in this zone was -0.7774965 °K.
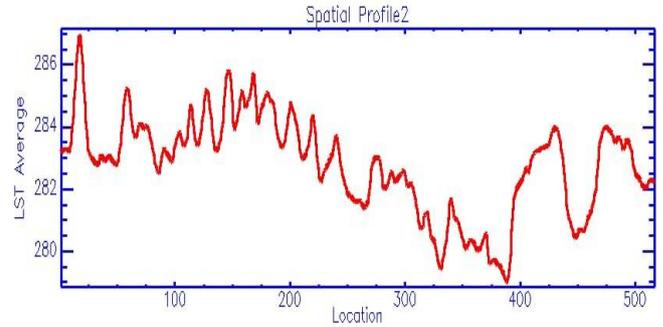
Fig. 12. Land surface temperature average change along on the Profile2.

The thermal anomalies zones in the study area are estimated via calculated the land surface temperature average gradient change to the presence of oil under the surface. From select two thermal anomalies zones, there are no traces of oil in profile 1 and profile 2 because the change of the land surface temperature in these zones anomalies is less than one Kelvin ($\Delta T < 1$ °K). The results of the two profiles can be summarized according to the Table IV.

TABLE IV. The results of the two regions can be summarized according to value of ΔT

Parameters \ Profiles	Profile1	Profile2
Start profile Lat.	31°28'35.25"N	31°14'15.81"N
Start profile Long.	130°20'55.67"E	130°48'46.14"E
End profile Lat.	31°28'35.54"N	31°14'15.96"N
End profile Long.	130°30'40.00"E	130°58'31.20"E
Cumulative Length profile	15.5 Km	15.6 Km
Euclidian Length profile	15.4 Km	15.5 Km
Max elevation	460 m	879 m
Min elevation	6.2 m	104 m
T_2	283.5131924 °K	282.6721610 °K
T_1	287.2096651 °K	283.4496575 °K
ΔT	-3.6964727 °K	-0.7774965 °K
Situation	There is unlikely any oil	There is unlikely any oil

At the last, the night-time scenes of the Thermal Infrared Sensor (TIRS) achieve a high gain of the thermal image with radiance 3.2-12.65 w/m²/μm/sr. Moreover, the analysis of the (TIRS) image is an optimal explanation for geomorphology and subsurface geology in the study area. The method used in this research achieved its objectives desired to improve model accuracy of oil exploration and for a large area in record time.

V. Conclusions

This study demonstrated the spectral recipe within thermal infrared (TIR) region of the electromagnetic (EM) radiation via thermal satellite imagery, geophysical data set, and isotopic analyses that aims to provide further understanding for the surface expressions of oil in the Kanoya province, and the coast of Kagoshima (the two regions are located in the south of Japan), which can be applied to identify the subsurface migration pathways for oil. So these phenomena provide useful information about the importance of these zones as a tool for the exploration of structures for oil. The night-time scenes of LDCM achieve high gains of the thermal image with radiance 3.2-12.65 (Watts/m^2 sr μm) when taken in ascending passages of the orbit, whereas the radiation anomalies can take different forms according to the surface expression of hydrocarbon. Moreover, the analysis of the LDCM image is an optimal explanation for geomorphology and surface geology in southern Japan via the potentiality of emulators set.

Acknowledgment

References

[1] Iolanda, I., Nadezhda, S., Janne, H., Henrik, V., and Daria, G., 2021. Satellite-based estimates of nitrogen oxide and methane emissions from gas flaring and oil production activities in Sakha Republic, Russia. Atmospheric Environment journal, X 1, 100114.

[2] Goldberg, L., Lu, Z., Streets, D.G., de Foy, B., Griffin, D., McLinden, A., Lamsal, N., Krotkov, A., and Eskes, H., 2019. Enhanced capabilities of TROPOMI NO$_2$: estimating NOx from North American cities and power plants. Environ. Sci. Technol. 53, 12594–12601.

[3] Yu, Q., Yi, G., Yi, W., and Zhen, G., 2020. Failure analysis on leakage of hydrogen storage tank for vehicles occurring in oil circulation fatigue test. Engineering Failure Analysis journal, Volume 117, 104830.

[4] Yonghwi, K., Marie, C., Odile, B., Amadou, S., and Jean, C. 2021. Identification and composition of carbonate minerals of the calcite structure by Raman and infrared spectroscopies using portable devices. Spectrochimica Acta Part A: Molecular and Biomolecular Spectroscopy, Volume 261, 119980.

[5] Roberto, R., Milagrosa, A., Vincenzo, C., Santiago, Y., and Cristina, A., 2021. The surface expression of hydrocarbon seeps characterized by satellite image spectral analysis and rock magnetic data (Falcon basin, western Venezuela). Journal of South American Earth Sciences, Volume 106, 103036.

[6] Saeid, A., and Carlos, R., 2020. Characterization of microseepage-induced diagenetic changes in the Upper-Red Formation, Qom region, Iran. Part 2: A new insight using reflectance spectroscopic analysis. Marine and Petroleum Geology 117. 104387.

[7] Michael, A., 2020. Microseepage vs. Macroseeepage: Defining Seepage Type and Migration Mechanisms for Differing Levels of Seepage and Surface Expressions. Adapted from an oral presentation given at AAPG Hedberg Conference, Hydrocarbon Microseepage: Recent Advances, New Applications, and Remaining Challenges, Houston, Texas, United States.

[8] Asadzadeh, S., and Souza, F., 2020. Characterization of microseepage-induced diagenetic changes in the Upper-Red Formation, Qom region, Iran. Part 1: Outcrop, geochemical, and remote sensing studies. Mar. Petrol. Geol. 113, 104149.

[9] Hacıoglu, O., Bas¸okur, A.T., Diner, H., Meqbel, N., Arslan, H.I., ˙ and Oguz, K., 2020. The effect of active extensional tectonics on the structural controls and heat transport mechanism in the Menderes Massif geothermal province: Inferred from threedimensional electrical resistivity structure of the Kurs¸unlu geothermal field (Gediz Graben, western Anatolia). Geothermics 85, 101708.

[10] Chakraborty, A. Mokudai, K. Cooper, M. Watanabe, M., and Chakraborty, S. 2018. Natural Heritage of Japan: Geological, Geomorphological, and Ecological Aspects. Springer. Switzerland. P: 87-131.

[11] Alexandra G., Paschalis D., and George F., 2021. Detecting geothermal anomalies using Landsat 8 thermal infrared remotely sensed data. International Journal of Applied Earth Observations and Geoinformation 96, 102283.

[12] Emetere, E., Sanni, E., Emetere, M., and Uno, U, 2017. Thermal infrared remote sensing of hydrocarbon in Lagos-southern Nigeria: application of the thermographic model. International Journal of geomate. 13 (39): 33-45.

[13] L. Feng, H. Tian, Z. Qiao, M. Zhao, and Y. Liu. 2020. Detailed variations in urban surface temperatures exploration based on unmanned aerial vehicle thermography. IEEE J. Sel. Top. Appl. Earth Observ. Remote Sens., vol. 13, pp. 204–216.

[14] Jiguang C., Man L., Zhitao Z., Shuqin Y., and Jifeng N., 2021. Robust UAV Thermal Infrared Remote Sensing Images Stitching Via Overlap-Prior-Based Global Similarity Prior Model. IEEE journal of selected topics in applied earth observations and remote sensing, vol 14.

[15] Artzai P., Aitor A., Jose A., Gabriel L., and Asier V. 2021. A Probabilistic Model and Capturing Device for Remote Simultaneous Estimation of Spectral Emissivity and Temperature of Hot Emissive Materials. IEEE Access, Volume 9, Page(s): 100513 – 100529.

[16] Diego U., Jose D., Luiz V., Clecia G., Veridiana S., Carlos C., Manuela P., and Wanderson M. 2020. Emissivity of agricultural soil attributes in southeastern Brazil via terrestrial and satellite sensors Geoderma journal, Volume 361, 114038.

[17] Lorente, A., Borsdorff, T., Butz, A., Hasekamp, O., Brugh, J., Schneider, A., Wu, L., Hase, F., Kivi, R., Wunch, D., Pollard, F., Shiomi, K., Deutscher, M., Velazco, A., Roehl, M., Wennberg, O., Warneke, T., and Landgraf, J., 2021. Methane retrieved from TROPOMI: improvement of the data product and validation of the first 2 years of measurements. Atmos. Meas. Tech. 14, 665–684.

[18] McLinden, A., Fioletov, V., Boersma, F., Kharol, K., Krotkov, N., Lamsal, L., Makar, A., Martin, V., Veefkind, P., Yang, K., 2014. Improved satellite retrievals of NO2 and SO$_2$ over the Canadian oil sands and comparisons with surface measurements. Atmos. Chem. Phys. 14, 3637–3656.

[19] Markowski, C. and Finkl, C., 2018. Threats to Mangrove Forests: Hazards, Vulnerability, and Management. 1st ed. London, United Kingdom: springer publishing, pg-55.

[20] Nelson, S. and Khorram, S., 2019. Image Processing and Data Analysis with ERDAS IMAGINE Image Processing and Data Analysis with ERDAS IMAGINE. 1st ed. United States: CRC (an imprint of Taylor and Francis Group, LLC), pg-241.

[21] Rui-Heng, S., Xiao-Peng H., Jian S., Hong Q., and Zun-Dong Y. 2021. Accurate numerical model for characteristic temperature acquisition of miniature fixed-point blackbodies. Measurement journal, Measurement 168, 108462.

[22] Imene, L., Mouloud T. 2017. Thermodynamic properties of the blackbody radiation: A Kaniadakis approach, Physics Letters A 381, 452–456.

[23] E. Gravanis and E. Akylas. 2021. Blackbody radiation, kappa distribution and superstatistics. Physica A: Statistical Mechanics and its Applications, Volume 578, 126132.

[24] Abdullah, A., Abdulla A., Abdullah, A., Kaniz A., Dewan J., Md, S., Tahera A., Saumik M., and Md, R. 2021. Assessing and predicting land use/land cover, land surface temperature and urban thermal field variance index using Landsat imagery for Dhaka Metropolitan area. Environmental Challenges Journal, 100192.

[25] Shunlin, L., Jindi, W. 2019. Advanced remote sensing-terrestrial information extraction and applications. Second edition, Academic Press is an imprint of Elsevier.